Analytica Chimica Acta 1232 (2022) 340488

Contents lists available at ScienceDirect

Analytica Chimica Acta

journal homepage: www.elsevier.com/locate/aca

A highly sensitive, easy-and-rapidly-fabricable microfluidic electrochemical cell with an enhanced three-dimensional electric field

Zhenglong Li [a], Yu-Hsuan Cheng [a], Charmi Chande [a], Sayandev Chatterjee [b], Sagnik Basuray [a,c,*]

[a] Department of Chemical and Materials Engineering, New Jersey Institute of Technology, Newark, NJ, 07102, United States
[b] TerraPower LLC, Bellevue, WA, 98008, United States
[c] Department of Biomedical Engineering, New Jersey Institute of Technology, Newark, NJ, 07102, United States

HIGHLIGHTS

- Simple protocol for constructing non-planar interdigitated microelectrodes (NP-IDμE).
- Three-dimensional electric field penetration in NP-IDμE based electrochemical cell (NP-μFEC).
- Lab-on-a-chip microfluidic platform for heavy metals detection in water matrices.

GRAPHICAL ABSTRACT

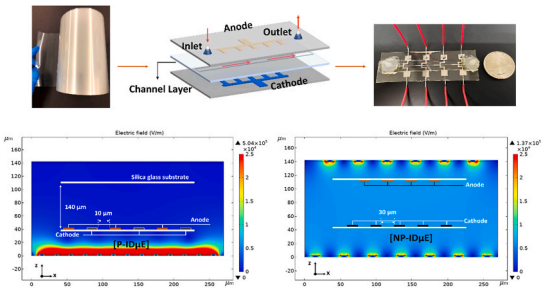

ARTICLE INFO

Keywords:
Non-planar interdigitated microelectrode
Electrochemical analytical tool
Finite element analysis
Heavy metals

ABSTRACT

An NP-μFEC is a reusable, novel microfluidic electrochemical cell with multiple non-planar interdigitated microelectrode arrays, minimal sample volume, and enhanced electric field penetration for highly sensitive electrochemical analysis. (**i**) The NP-μFEC features spatial 3-electrode architecture, and a small sample volume (~4 μL). (**ii**) Here, $[Fe(CN)_6]^{3-/4-}$ redox couple are used as an electrochemical reporter. The effects on the electrochemical properties of NP-μFEC due to the change in the reference electrode (RE) and counter electrode (CE)'s position with respect to the working electrode (WE) position are analyzed. For NP-μFEC, the position of the RE with respect to the WE does not affect the CV, DPV electrochemical profiles. However, the spacing between the CE and WE plays a significant role. (**iii**) The enhanced three-dimensional electric field penetration in NP-μFEC is validated by finite element analysis simulation using COMSOL Multiphysics. (**iv**) Without electrode surface modifications, NP-μFEC shows a detection limit (***DL***) of $\sim 2.54 \times 10^{-6}$ M for aqueous $[Fe(CN)_6]^{3-/4-}$ probe. (**v**) The ***DL*** for Cu^{2+}, Fe^{3+}, and Hg^{2+} are 30.5±9.5 μg L^{-1}, 181±58.5 μg L^{-1}, and 12.4±1.95 μg L^{-1}, respectively, which meets the US Environmental Protection Agency (EPA)'s water contamination level for Cu, Fe, and is close to that for Hg (EPA limits are 1300 μg L^{-1}, 300 μg L^{-1}, and 2 μg L^{-1}, respectively). (**vi**) Further, using a pressure-sensitive adhesive layer to form the channel and create the NP-μFEC configuration simplifies the manufacturing process, making it cost-effective and allowing for rapid adoption in any research lab. NP-μFEC is used to detect heavy metal ions in water. This demonstrates that cost-effective, easy-to-fabricate NP-μFEC can be a new sensitive electrochemical platform.

* Corresponding author. Department of Chemical and Materials Engineering, New Jersey Institute of Technology, Newark, NJ, 07102, United States.
E-mail address: sbasuray@njit.edu (S. Basuray).

https://doi.org/10.1016/j.aca.2022.340488
Received 25 April 2022; Received in revised form 21 September 2022; Accepted 4 October 2022
Available online 7 October 2022

1. Introduction

Rapid, cost-effective, highly sensitive, and label-free detection characteristics of microfluidic electrochemical cells (μFECs) are receiving increasing attention [1–3]. In the past decades, significant efforts have been made to design and optimize μFECs' electrode architecture to fabricate analytical devices with high sensitivity, accuracy, and reproducibility [4–6]. Microelectrodes (μEs), an essential component in μFECs, offer higher sensitivity than macroelectrodes of conventional size due to their smaller area-edge effects [4]. Various μE geometries have been evaluated and applied to μFECs [7–9]. A pair of comb-like metal electrodes on a planar insulating substrate, as shown in Fig. 1(a), is called planar interdigitated microelectrodes (P-IDμEs). The interdigitated layout of the electrode fingers endow P-IDμEs with promising advantages, e.g., the fast establishment of the steady-state, low ohmic drop, and increased signal-to-noise ratio [1,4]. However, for the P-IDμEs, the electric field is chiefly localized near the μE surface (two-dimensional (2D) electric field), as shown in Fig. 1(b) [10,11]. The 2D electric field limits the penetration of the electric field, leading to a loss in sensitivity for P-IDμE, specifically for impedance-based sensing [12–14].

Researchers have employed different methodologies to address this problem, such as (**i**) including nanomaterials to increase the active electrode surface area or (**ii**) designing elaborate device structures [15–18]. It is shown by Noda et al. that CNT forests on μEs significantly enhance transducer detection performance [15]. For Noda et al., the P-IDμE-based transducer sensitivity improved considerably by extending the "active detection area" using carbon spacer/carbon nanostructures. Morallon and co-workers employed a μFEC with hybrid μEs comprised of graphene oxide decorated with gold nanoparticles to successfully detect uric acid and ascorbic acid in urine samples at detection limits of 0.62 μM and 1.4 μM, respectively [16]. Recently, Bratov et al. introduced the concept of three-dimensional (3D) IDμE with electrode fingers separated by an insulating SiO_2 barrier [10,17]. This 3D electrode architecture prolongs the current transmission path along the barrier's surface, enhancing the device's sensitivity toward probing reactions of biomolecules attached to the barrier surface. However, all of the above μFEC and others in the literature require complicated, time-consuming, and expensive device construction processes despite the mentioned advantages [18,19].

Our previous papers demonstrated that packing a 2-electrode non-planar IDμE (NP-IDμE) based μFEC platform (hereafter NP-μFEC) allows us to use it as an excellent electrochemical impedance transducer [20,21]. The 2-electrode NP-μFEC is a sensitive affinity-based impedance sensor that uses electrochemical impedance spectroscopy (EIS), which has enhanced 3D electric field penetration. However, detection of molecules that lack suitable capture probes (like dopamine, uric acid, and heavy metals), EIS cannot be used as the detection mode. Therefore, for detecting these molecules, the electrochemical behavior of NP-μFEC, specifically in the DC modes (like cyclic voltammetry (CV) and differential pulse voltammetry (DPV)), needs to be characterized and fundamentally examined. Therefore, inspired by our previous 2-electrode design, to check the application capability of NP-μFEC in the DC detection modes (CV, DPV), a new 3-electrode NP-μFEC is proposed in this work. Here, a fundamental study using simulations and experiments is undertaken to visualize and demonstrate the new 3-electrode NP-μFEC as an analytical tool. Unless otherwise noted, the NP-μFEC appearing hereafter means the 3-electrode NP-μFEC.

The characteristics of the NP-μFEC are a small sample volume (~4 μL), reusability, easy assembly, and enhanced 3D electric field. Furthermore, to understand and check the applicability of NP-μFEC, especially for the DC working modes (CV and DPV), a series of electrochemical comparisons between NP-μFEC and regular P-μFEC are fundamentally examined. Furthermore, COMSOL modeling of the electric field in both NP-μFEC and regular P-μFEC is done to critically examine the effect of the electric field on the electrochemical data. Finally, based on the fundamental understanding of the physicochemical characteristics of NP-μFEC, an optimized channel height of NP-μFEC is used for the highly sensitive detection of heavy metal ions in aqueous solutions.

Current microfluidic electrochemical platforms with 3D electrodes suffer from complicated, time-consuming, and expensive construction [10,17]. Here, the NP-μFEC is proposed that overcomes the current limitations mentioned above. In summary, the NP-μFEC platform described here has the following advantages over existing platforms in literature:

(1) **Fabrication:** NP-μFEC consists of three layers, a top and bottom glass layers decorated with μE arrays and a middle double-sided polyester-based pressure-sensitive adhesive (PSA) layer with the desired channel pattern (60 mm × 500 μm x 140 μm in length x width x height, respectively) sandwiched between μE layers. This

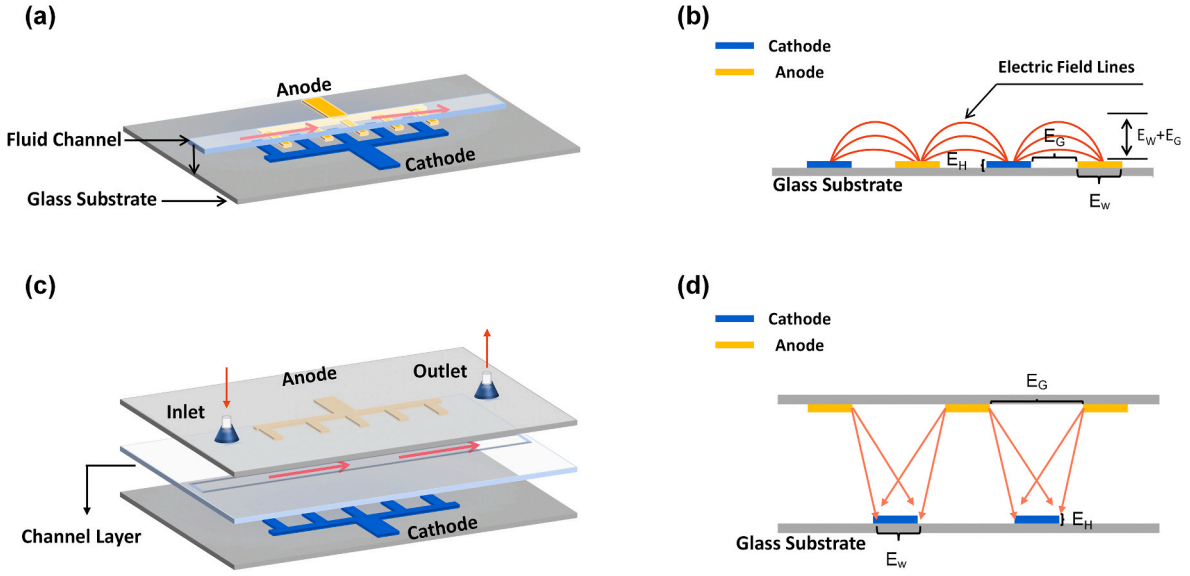

Fig. 1. (a) Schematic diagram of P-IDμE. (b) Distribution of electric fields within P-IDμE. Here, E_H, E_W, E_G represents the electrode height, width, and gap between adjacent electrode fingers, respectively. (c) Schematic diagram of the NP-IDμE and (d) its corresponding electric field distribution.

strategy allows constructing of a μFEC configuration without extensive fabrication while having a small sample volume (~4 μL) [22]. The detailed fabrication protocols of μE and NP-μFEC are shown in Figs. S1 and S2, respectively. Further, the PSA layer provides the advantages of (**i**) a reasonably wide operating temperature window (−40 °C–120 °C), (**ii**) fast and easy electrode assembly, and (**iii**) excellent reagent-resist properties. Thus, the fabrication process of NP-μFEC is simple, cost-effective, and accelerates NP-μFEC adoption as an alternative to P-μFEC by other research groups.

(2) **3D Electric Field:** An advantage of the NP-μFEC is allowing a vertical distributed electric field. The spatial orientation of the μE arrays enables the electric field to penetrate through the whole channel layer. As a result, the electric field is no longer confined to the μE surface, which tremendously increases the sensitivity of impedance sensors (Fig. 1(d)). Furthermore, any changes between the μE layers will contribute to the final output signal even without electrode or channel modifications [20,21].

(3) **Fully Integrated:** It is well documented that any alterations and modifications in electrode design, such as the distances between the electrodes (working electrode (WE), counter electrode (CE), and reference electrode (RE)) and their relative positions can significantly alter electrochemical systems and lead to a drop in device performance [23–26]. Furthermore, previous studies demonstrated that an internal RE positioned inside the microchannel benefits μFECs' sensitivity because of a smaller ohmic drop [27,28]. Therefore, in this work, the NP-μFEC with four pairs of NP-IDμE arrays inserted within a single microfluidic channel is ideally suited for electrochemical characterizations. The electrochemical behavior of the NP-μFEC is compared against a conventional P-μFEC using a well-known redox probe potassium Ferri/ferrocyanide ($K_3/K_4Fe(CN)_6$). It is essential to note that the solution is static (no flow) to exclude the contribution of forced convection. Under this static condition, the effect of the distance between the electrodes (WE, CE, and RE) and their final positions on the electrochemical behavior of NP-μFEC are studied in detail. Finite element analysis (FEA) using COMSOL Multiphysics 5.5 is adapted to visualize the electric field distribution between the NP-μFEC vs. P-μFEC. (**i**) Comparisons between the NP-μFEC and P-μFEC demonstrate that the transformation in electrode architecture leads to linear diffusion-controlled redox processes in NP-μFEC in contrast to a radial diffusion behavior in P-μFEC. For NP-μFEC, the RE's position does not affect the CV and DPV electrochemical profiles. However, the spacing between the CE and WE significantly affects the electrochemical behavior. (**ii**) COMSOL Multiphysics validates enhanced 3D electric field penetration in the NP-μFEC. (**iii**) Without any electrode surface modifications (like metal nanoparticles or CNT), the NP-μFEC shows a detection limit (***DL***) of ~2.54×10^{-6} M for aqueous $[Fe(CN)_6]^{3-/4-}$ probe, which is similar to that of the P-μFEC (~1.8×10^{-6} M). Thus it can be concluded that, even though the transition of μE arrays from planar distribution to non-planar distribution will increase the diffusion distance of ions, this does not significantly influence the μFEC's performance.

An anomalous lowering of ***DL*** is seen with increasing channel height of NP-μFEC till it reaches a critical height (420 μm), beyond which the ***DL*** increases with an increase in channel height. Therefore, the DL of Cu^{2+}, Fe^{3+}, and Hg^{2+} was determined to evaluate the potential and performance of NP-μFEC as an electrochemical platform at 420 μm channel height. The ***DL*** of NP-μFEC for Cu^{2+}, Fe^{3+}, and Hg^{2+} are 30.5± 9.5 μg L^{-1}, 181±58.5 μg L^{-1}, and 12.4±1.95 μg L^{-1}, respectively, which meets the US Environmental Protection Agency (EPA)'s water contamination level for Cu, Fe and is close to that for Hg (1300 μg L^{-1}, 300 μg L^{-1}, and 2 μg L^{-1}, respectively). Therefore, this demonstrates that our cost-effective, easy-to-fabricate NP-μFEC can be an ideal new electrochemical analytical tool for other research groups.

2. Experimental section

2.1. Materials and chemicals

Potassium chloride (KCl) and potassium Ferri/ferrocyanide ($K_3/K_4Fe(CN)_6$) are purchased from Sigma-Aldrich. Mercury (II) chloride (98+%), Copper (II) chloride dihydrate (99+%), and Tris (2,2'-bipyridyl)ruthenium(II) chloride hexahydrate (≥98%) are purchased from Thermo Scientific. Iron (III) chloride (anhydrous, 98+%) is obtained from Alfa Aesar. The de-ionized (DI) water used in the experiments is obtained from a Milli-Q® Direct 8 Water Purification System. Acetone (≥99.5%, ACS) and isopropyl alcohol (99%, ASC) purchased from VWR Chemicals BDH® are used to clean chips. Sulfuric acid (H_2SO_4, Catalog No.A300C-212) and hydrogen peroxide (H_2O_2, Catalog No.H312-500) are acquired from Fisher Scientific™ and used for the removal of organic contaminants [29]. Hexamethyldisilazane (HMDS) and AZ 1512 are obtained from MicroChem Corp and used to prepare photoresist layers. AZ300 MIF developer is supplied by EDM Performance Materials Corp and used to make the underlying pattern visible in the developing process. Finally, a double-sided PSA tape (ARcare® 90106NB) from Adhesives Research, Inc. is adopted to use both an intermediate fluid channel and an adhesive layer to bond the top and bottom Pt μE layers. The glass substrate is from Globe Scientific Incorporated.

2.2. Electrochemical characterizations

$K_3[Fe(CN)_6]$ and $K_4[Fe(CN)_6]$ (1:1, mole ratio) redox couple in KCl (1 M) are used to assess the electrochemical performance of this novel non-planar system. The CV, EIS, and DPV signals are obtained using a Gamry (Reference 600+) potentiostat. Since platinum (Pt)-based RE provides a good option due to its longevity and easy fabrication, all electrodes (WE, CE, RE) are Pt, as shown in Fig. 2 [30]. For the DPV testing, the Step Size and the Pulse Size are 10 and 25 mV, respectively. The Sample Period is 1s, and the Pulse Time is 0.1s.

3. Results & discussion

The distances between the electrodes (WE, CE, and RE) and their relative placements are essential parameters for measuring the performance and reliability of NP-μFEC. The NP-μFEC has four sets of non-planar IDμE arrays. The length of one entire μE array is 10 mm, and the horizontal distance between adjacent μE arrays is ~4 mm, as shown in Fig. 2 (a). The P-μFEC has two sets of planar IDμE arrays. The length of one μE array is 10 mm, and the horizontal distance between adjacent μE arrays is ~6 mm, as shown in Fig. 2(g). Table 1 summarizes the geometric details of the Pt μE arrays. Different combinations of the μE arrays are used as WE, CE, and RE to study the relationship between electrochemical characterization techniques like CV, DPV, and EIS with changing distances between the WE, CE, and RE.

3.1. CV characterization

3.1.1. NP-μFEC CV

The voltammetric behavior for different μE configurations is shown in Fig. 2. The corresponding background currents are shown in Fig. S3. As shown in Fig. 2(d), for the WE/CE_1/RE_1 configuration, the voltammogram of 10 mM $K_3[Fe(CN)_6]$ and $K_4[Fe(CN)_6]$ (1:1, mole ratio) in KCl (1 M) at a scan rate (***ν***) of 100 mV s^{-1} shows oxidation at anodic peak potential (E_{pa}) of 75 mV and a back reduction at cathodic peak potential (E_{pc}) at −75 mV vs. Pt RE, such that the peak-to-peak separation (ΔE_p) is ca. 150 mV. As ***ν*** is increased, E_{pa} values move to more positive values while E_{pc} potentials are shifted to more negative values, increasing the

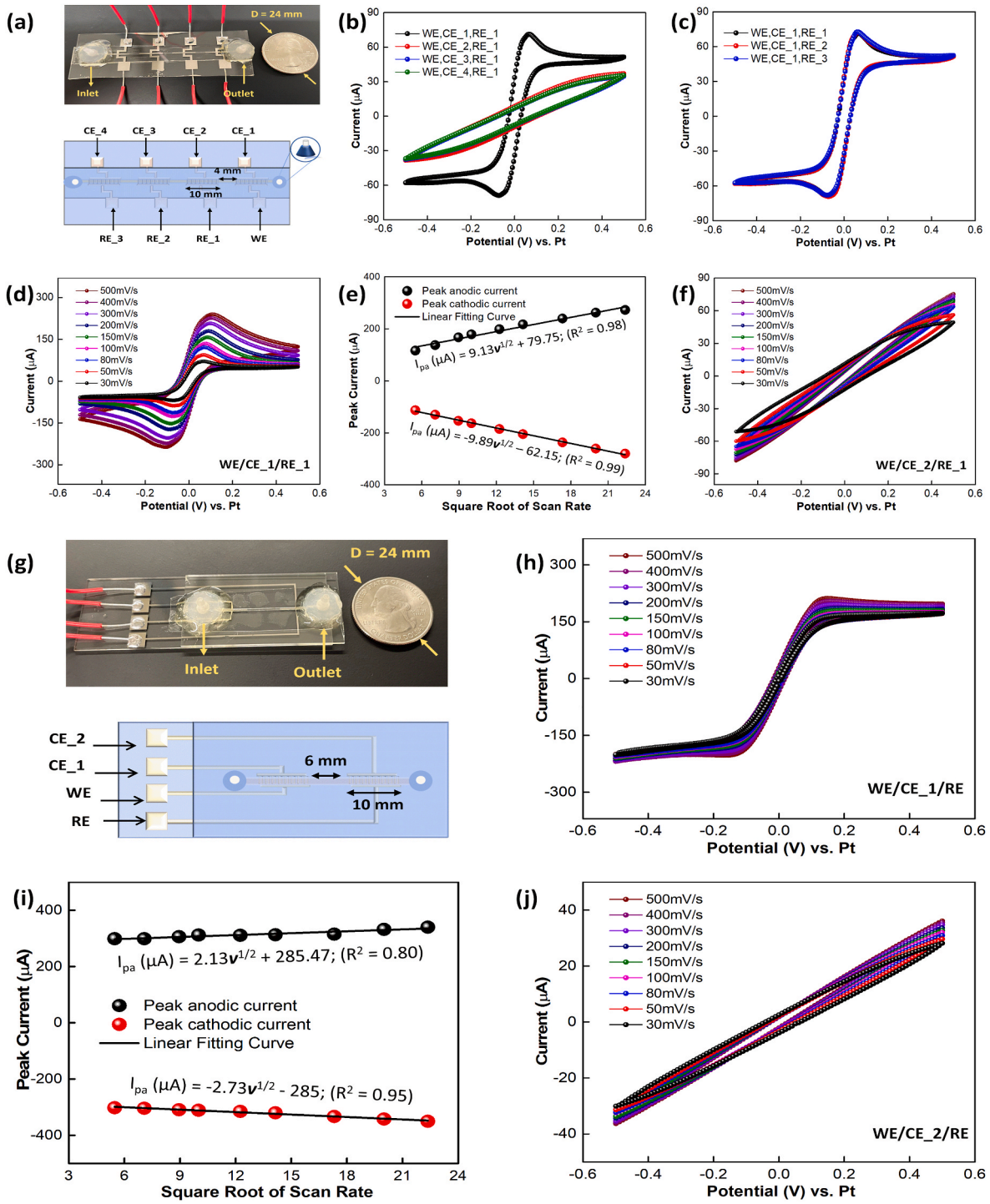

Fig. 2. (a) Picture (top) and schematic diagram (bottom) of NP-μFEC. Results (b)–(f) are obtained based on NP-μFEC. Here, the solution is $[Fe(CN)_6]^{3-/4-}$ (0.01 M) in KCl (1 M). (b) CV results at different CE positions with ν = 30 mV s^{-1}. (c) CV results at different RE positions with ν = 30 mV s^{-1}. (d) CV results under different ν based on WE/CE_1/RE_1 configuration. (e) Peak current plots (I_{pa}, I_{pc}) versus the square root of scan rates ($\nu^{1/2}$). The equation of the anodic peak current (I_{pa}) line: I_{pa} (μA) = 9.13 × $\nu^{1/2}$ + 79.75; Coefficient of determination (R^2) = 0.98. The equation of the cathodic peak current (I_{pc}) line: I_{pc} (μA) = −9.89 × $\nu^{1/2}$–62.15; R^2 = 0.99. (f) CV results under different ν based on WE/CE_2/RE_1 configuration. (g) Picture (top) and schematic diagram (bottom) of P-μFEC. Results (h)–(j) are acquired based on P-μFEC. Here, the solution is $[Fe(CN)_6]^{3-/4-}$ (0.01 M) in KCl (1 M). (h) CV results under different ν based on WE/CE_1/RE configuration. (i) Peak current plots (I_{pa}, I_{pc}) versus $\nu^{1/2}$. The equation of I_{pa} line: I_{pa} (μA) = 2.13 × $\nu^{1/2}$ + 285.47; R^2 = 0.80. The equation of I_{pc} line: I_{pc} (μA) = −2.73 × $\nu^{1/2}$–285; R^2 = 0.95. (j) CV results obtained at different ν based on WE/CE_2/RE configuration.

magnitude of ΔE_p ($(\Delta E_p$ @ ν):170 mV @ 150 mV s^{-1}; 210 mV @ 400 mV s^{-1}). Conversely, lowering ν results in decreasing ΔE_p (ΔE_p = 125 mV @ ν = 30 mV s^{-1}). In all cases, the apparent formal potential $E^{0'}$ of $[Fe(CN)_6]^{3-/4-}$ at the Pt WE are equal to $(E_{pa} + E_{pc})/2$ = ~0 mV and independent of ν.

The effect of ν on peak currents of the cyclic voltammograms is also monitored. It is observed that for all the ν studied, the ratio of the cathodic and anodic processes' peak currents (I_{pc}/I_{pa}) is consistently nearing 0.95, indicating the chemical reversibility as expected for the $[Fe(CN)_6]^{3-/4-}$ redox process. Furthermore, as shown in Fig. 2(e), from

Table 1
Parameter setting for COMSOL simulation.

Parameter	Value
Electrode Height (E_H)	0.1 μm
Electrode Width (E_W)	10 μm
Solution Electrical Conductivity	~9 S m^{-1}
Solution Relative Conductivity	80
Glass Substrate Electrical Conductivity	1×10^{-15} S m^{-1}
Glass Substrate Relative Permittivity	4.68
P-μFEC Double Layer Capacitance	~2.6×10^{-6} F
NP-μFEC Double Layer Capacitance	~1.6×10^{-6} F

30 to 500 mV s^{-1}, peak currents (I_{pa}, I_{pc}) vs. square root of scan rate ($\nu^{1/2}$) show good adherence to linearity, demonstrating classical Nernstian diffusion-controlled redox behavior [3,31,32].

$$i_p = 0.446nFAC^o\left(\frac{nF\nu D_0}{RT}\right)^{1/2} \quad (1)$$

The Randle-Sevcik Equation (1) can calculate the cumulative active electrode surface area (A_{real}). Using the literature value of diffusion coefficients (7.3×10^{-6} cm^2 s^{-1} for $[Fe(CN)_6]^{3-}$ [31]; 6.3×10^{-6} cm^2 s^{-1} for $[Fe(CN)_6]^{4-}$ [32]), the corresponding A_{real} are determined as 4.37×10^{-2} cm^2 and 4.62×10^{-2} cm^2, respectively. These calculated values agree with the actual cumulative geometrical surface area (A_{geom}, ~1.25×10^{-2} cm^2) of Pt WE.

3.1.2. Influence of RE and CE's relative placement on NP-μFEC CV

Keeping the WE and CE positions the same and altering the RE's position (WE/CE_1/RE_1,2,3) does not affect the redox behavior, as demonstrated by the near-identical voltammograms in Fig. 2(c). However, in conventional bulky 3-electrode systems, the position of RE relative to the WE is observed to significantly impact the potential drop (iR_{cell}) between the RE and WE. Therefore, positioning the RE close to the WE is recommended in such set-ups for precise control over the WE potential [33–35]. However, in NP-μFEC, no noticeable impact of the RE position alterations relative to WE is observed even when the distance between the RE and WE (d_{rw}) is as long as ~ 32 mm (when RE is at RE_3), suggesting higher electrochemical operational flexibility in NP-μFEC.

However, significant changes are observed when the CE's position is progressively offset from the WE, as demonstrated in Fig. 2(b) and (f). Upon switching from WE/CE_1/RE_1 to WE/CE_2/RE_1, the current curves show significantly less prominent redox features and a considerable reduction in the overall current intensity. The voltammograms with WE/CE_2,3,4/RE_1 configuration show similar behavior, as shown in Figs. S3(c) and (d). However, with an increase in the scanning range from (+550 to −550 mV) to (+900 to −900 mV), redox peaks are reobserved (Fig. S3(e)). Fig. S4 shows the CV results obtained at different CE positions. Compared with other configurations, for WE/CE_1/RE_1 (WE and CE are interdigitated), well-defined cyclic voltammograms with relatively narrower ΔE_p and high peak currents are obtained. However, for WE/CE_2,3,4/RE_1 (WE and CE are non-interdigitated), massive shifts in peak potentials (E_{pa}, E_{pc}) are observed with the increase of concentration, and these results in considerable gains in ΔE_p (Table S1). This usually indicates a high barrier to electron transfer, and electron transfer reactions are sluggish [36]. Hence more negative (positive) potentials are required to observe reduction (oxidation) reactions, giving rise to more significant ΔE_p.

Figs. S5 and S6 show that the ohmic drop iR_{cell} between RE_1/2/3 and WE is approximately 5.4 mV, 7.4 mV, and 9.6 mV, respectively. Since there are no apparent changes in the ohmic drop, there are no/minimal changes in the cyclic voltammograms (Fig. 2(c)). However, dramatic changes are observed with the increase of the spacing between the CE and WE (d_{cw}), as exemplified by the loss of the classical "duck-shape" features of cyclic voltammograms. When the CE and WE are increasingly offset, the ohmic drop between the CE and WE increases from ~2.3 to 45.6 mV (Fig. S7). Therefore, in NP-μFEC, the spacing d_{cw} plays a more critical role than the d_{rw} on the NP-μFEC's electrochemical performance.

In addition, since the cyclic voltammograms are obtained under the stagnant condition, convective contribution to the overall current density can be ignored. Furthermore, at the high ionic strength liquid of 1 M KCl, the contribution of electromigration can also be neglected [28]. Hence, mass transport is chiefly dominated by diffusion. With the stepwise movement of CE away from the WE, the diffusional gradient of reagents/products weaken significantly. This will decrease the current density leading to poor electrochemical performance. All these findings suggest that in NP-μFECs, the interdigitated layout of the CE and WE is the best option for CV and DPV. This provides us with valuable preliminary suggestions on the future design or optimization of the NP-μFEC as an analytical tool.

3.1.3. P-μFEC CV

The promising results observed in NP-μFEC motivated us to contrast the CV results of NP-μFEC against P-μFEC. Fig. 2(g) is the schematic diagram of the P-μFEC configuration. The voltammetric responses of two different electrode configurations (WE/CE_1/RE and WE/CE_2/RE) are studied and shown in Fig. 2(h) and (j), respectively. The corresponding background currents are shown in Fig. S8(a).

3.1.4. Influence of RE and CE's relative placement on P-μFEC CV

For the WE/CE_1/RE configuration, the *I* (current) vs. *E* (applied potential) profile at $\nu = 100$ mV s^{-1} shows a sigmoidal behavior reminiscent of a steady-state electrochemical process characteristic of a predominantly radial diffusion field [23,37,38]. In this case, $[Fe(CN)_6]^{3-/4-}$ get reduced/oxidized between the WE and CE electrode fingers. This process is sometimes referred to as redox cycling. A key observation is that ΔE_p decreases in magnitude gradually as the ν is progressively increased ($(\Delta E_p$ @ $\nu)$: 360 mV @ 30 mV s^{-1}; 330 mV @ 100 mV s^{-1}; 280 mV @ 500 mV s^{-1}), as shown in Fig. S8(b). This behavior of the P-μFEC marks a stark contrast to the NP-μFEC, which shows an opposite trend in the variations of ΔE_p with ν. By contrast, the formal potential $E^{0'}$ of $[Fe(CN)_6]^{3-/4-}$ in the P-μFEC equals ~ 0 mV and therefore mirrors the behavior of NP-μFEC in being ν independent. The effects of ν on the peak currents in the cyclic voltammograms are illustrated in Fig. 2(i). The linear relationship between the peak currents (I_{pa}, I_{pc}) and $\nu^{1/2}$ further confirms a classical Nernstian behavior in P-μFEC, where diffusion is the rate-limiting step [1]. The Randle-Sevcik Equation (1) can estimate the cumulative WE surface area, A_{real} [39]. The value of A_{real} estimated using the Randle-Sevcik analyses on the cathodic processes and the anodic processes are equal to 1.14×10^{-2} cm^2 and 1.25×10^{-2} cm^2, respectively, which is consistent with the actual cumulative working electrode surface area A_{geom} of 1.25×10^{-2} cm^2.

Fig. 2(j) shows the CV test results obtained at WE/CE_2/RE under different scan rates. Significantly less prominent redox features and reduced current intensities are observed when the CE is fixed at CE_2. By comparing the results in Fig. 2(h) and (j), it is also found that in the P-μFEC, when the spacing d_{cw} is decreased to ~ 10 μm, that is, WE and CE are interdigitated, well-defined CV curves appear. This finding further confirms the previous assumption that for both P-IDμE and NP-IDμE based μFECs, the spacing d_{cw} plays a more critical role in the final electrochemical performance.

3.1.5. NP-μFEC vs. P-μFEC

Based on the analysis above, the difference in the electrochemical characteristics between the NP-μFEC and P-μFEC (when the CE and WE are interdigitated) is:

(i) Different electrochemical processes: NP-μFEC demonstrates a semi-infinite linear diffusion, while the P-μFEC shows radial diffusion. However, the semi-infinite linear diffusion enables NP-μFEC one significant benefit: it can easily interrogate the valuable

information related to redox processes (like E_{pa}, E_{pc}, I_{pa}, I_{pc}), while for P-μFEC is challenging.

(ii) Different peak-to-peak separation (ΔE_p) behavior: Interestingly, for both NP-μFEC and P-μFEC, ΔE_p changes slightly with *v*. It is hypothesized that this deviation could be due to slow electron transfer to the bare μEs [39]. However, for NP-μFEC, ΔE_p increases with *v*, while for P-μFEC, ΔE_p decreases with *v*. From Table S4, it is found that for NP-μFEC, the overall intensity in ΔE_p is much smaller than that of the P-μFEC. This relatively narrower ΔE_p means a higher charge-transfer ability is observed in the non-planar configuration [40].

3.2. COMSOL multiphysics simulation

For both planar and non-planar μFEC, to see changes in the electric fields as the CE and WE are more and more offset from each other and compare the difference in the electric field distribution in the NP-μFEC and P-μFEC. Detailed FEA using COMSOL Multiphysics 5.5. is carried out to determine the actual electric field distribution within the NP-μFEC vs. P-μFEC. In addition, FEA is also employed to see the influence of the transition in μE arrays (from coplanar to non-planar interdigitated structure) on the distribution of concentration profiles of aqueous $[Fe(CN)_6]^{3-/4-}$ couple.

Table 1 summarizes the simulation parameters. The effect of double-layer capacitance is considered in the COMSOL simulation. And relevant double-layer capacitance values are obtained based on EIS results (Tables S3 and S5). To avoid long pre-processing, solving, and post-processing periods, the geometries of the P-μFEC and NP-μFEC are simplified to a representative 2D model, as shown in Fig. 3(a) [41]. Besides, the periodic distribution characteristics further reduce the model to a few representative pairs of electrode fingers. The gap (E_G) of the planar IDμE arrays is set to 10 μm, while the E_G of non-planar IDμE arrays is set to 30 μm to ensure a consistent number of electrode fingers per unit length in these two electrode structures. Of note, the electric field distribution in the P-μFEC and NP-μFEC at a potential drop of +1.0 V vs. Pt is taken as an example. The electric field distribution is recorded and plotted across the whole microfluidic channel, as Fig. 3(b)–(d) demonstrates. Fig. 4 shows the corresponding spatial distribution of the electric field in the P-μFEC and NP-μFEC.

3.2.1. P-μFEC 2D electric field distribution

From the simulation results, the P-μFEC and NP-μFEC display different electric field distributions. For the P-μFEC, the electric field is concentrated near the electrode surface, akin to a 2D-like distribution, as shown in Figs. 3(b) and 4(a, b). Higher electric field intensity (I_{EF}) is observed at the edges of electrode fingers because of edge effects [42]. Fig. 3(b) shows us that the penetration of the electric field (in the z-axis) is around 20 μm in the P-μFEC, which matches the value of E_W (10 μm) + E_G (10 μm) and is consistent with the literature [11,43,44]. A radial distributed electric field is observed from the local magnification diagram of Fig. 3(b). However, most regions within the microfluidic channel layer show almost negligible I_{EF}.

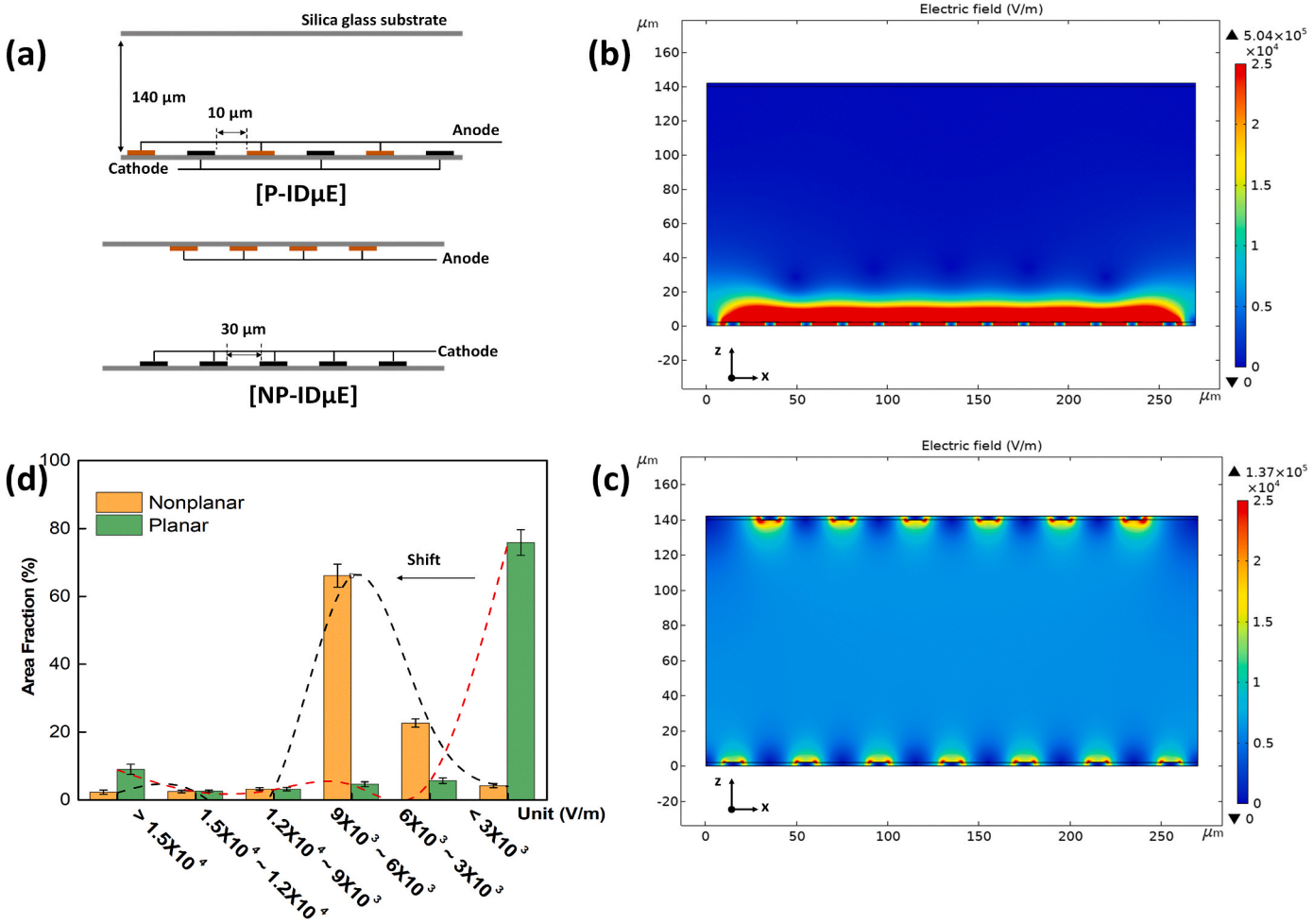

Fig. 3. (a) Cross-section μE configuration of P-μFEC (top) and NP-μFEC (bottom). Simulated electric field distribution within P-μFEC (b) and NP-μFEC (c) channel. (d) Distribution of the effective area fractions with different I_{EF} intervals within P-μFEC and NP-μFEC channels. Black (Nonplanar) and red (Planar) dotted lines represent the corresponding fitted curves. (For interpretation of the references to colour in this figure legend, the reader is referred to the Web version of this article.)

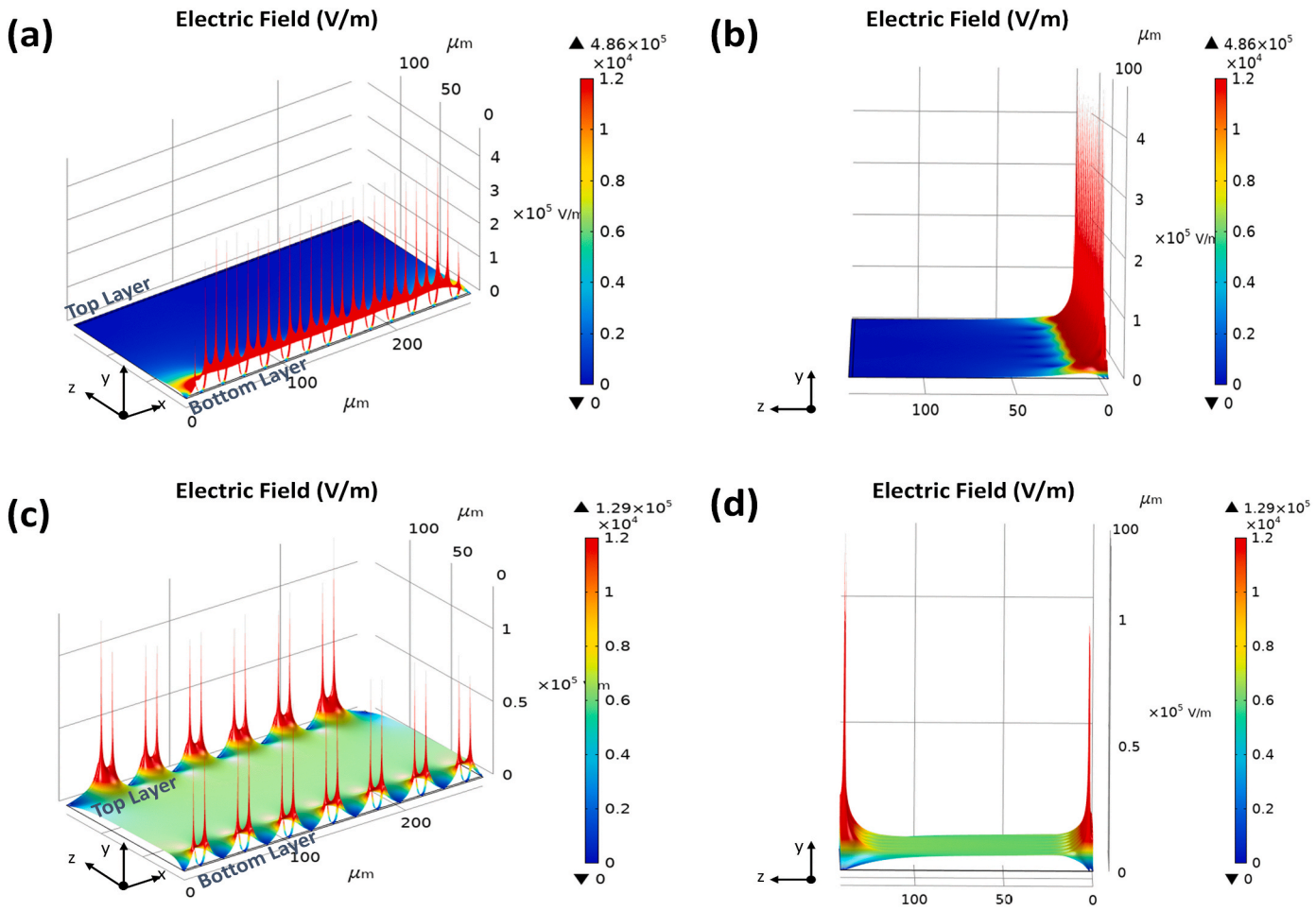

Fig. 4. (a) and (b) represent the spatial distribution of the electric field (from different angles) in P-μFEC. (c) and (d) describe the spatial distribution of the electric field (from different angles) in NP-μFEC.

3.2.2. *NP-μFEC 3D electric field distribution*

For the NP-μFEC, the μE arrays' spatial orientation lets the opposite electric field penetrate each other. Furthermore, the electric field is no longer confined to the μE surface (Figs. 3(c) and 4(c, d)). Instead of seeing a radial distributed electric field, a vertically channel-wide electric field appears in NP-μFEC. As a result, a more uniformly distributed electric field with enhanced intensity across the entire microfluidic channel volume is observed. This imparts NP-μFEC with higher electrochemical sensitivity than its corresponding planar counterpart as an impedance transducer.

3.2.3. *P-μFEC vs. NP-μFEC*

The channel layer of the P-μFEC and NP-μFEC have been divided into six regions with different I_{EF} intervals to facilitate analysis and comparison between them (Fig. 3(d)). The locations of these six regions with varying intervals of I_{EF} in the P-μFEC and NP-μFEC are shown in Figs. S10 and S11, respectively. Table S6 summarizes their corresponding cross-section area fractions. It is found that the P-μFEC has more channel area falling in a relatively stronger electric field range ($>1.5 \times 10^4$ V m^{-1}) than that in NP-μFEC. However, most of the channel layer (~75.77%) has a weak electric field strength ($<3 \times 10^3$ V m^{-1}). For the NP-μFEC, most of the channel (~66.00%) falls in a moderate electric field intensity region (from 9×10^3 to 6×10^3 V m^{-1}).

This FEA study shows us that the transition of μE arrays from planar distribution to non-planar distribution will "drag" a significant part of the electric field away from the μE surface to the bulk channel, as shown in Fig. 3(d). It is also observed that with the stepwise separation between the CE and WE, the electric fields in both the P-μFEC and NP-μFEC undergo a severe attenuation, as shown in Figs. S12 and S13. Time-dependent mass transport simulations across the channel of NP-μFEC and P-μFEC are conducted using Butler-Volmer electrode kinetics (Fig. S14). The simulated concentration profiles indicate a redox cycling in P-μFEC and a linear diffusion process in NP-μFEC. These findings are consistent with the observed CV results.

3.3. *EIS characterization*

As shown above, in both P-μFEC and NP-μFEC, the stepwise separation between the CE and WE dramatically decreases the I_{EF}. Therefore, it is expected that the severe decrease in I_{EF} should lead to dramatic increases in the charge transfer resistance (R_{ct}). EIS characterization is thus conducted to visualize the changes in R_{ct} due to the stepwise separation between the CE and WE for both P-μFEC and NP-μFEC.

3.3.1. *NP-μFEC EIS*

The proposed equivalent circuit in Fig. 5(a) models the EIS signature (Nyquist Curve). In this equivalent circuit in Fig. 5(a), *L* is the parasitic inductor in the device due to external noises. Since the external circuit's resistance is ordinarily negligible, it is not considered in Fig. 5(a). R_c represents the resistance of the solution filling between the WE and CE. C_c is the cell capacitance originating from the NP-IDμE electrochemical cell. Instead of an ideal double-layer capacitance (C_{dl}), the constant phase element *Q* is employed due to the inhomogeneity of the interface between the Pt μE and electrolyte [3,45]. R_{ct} is the charge transfer resistance associated with the electrons' transfer from the electrolyte onto the μE [45]. The Warburg element (*W*) impedes the reactants'

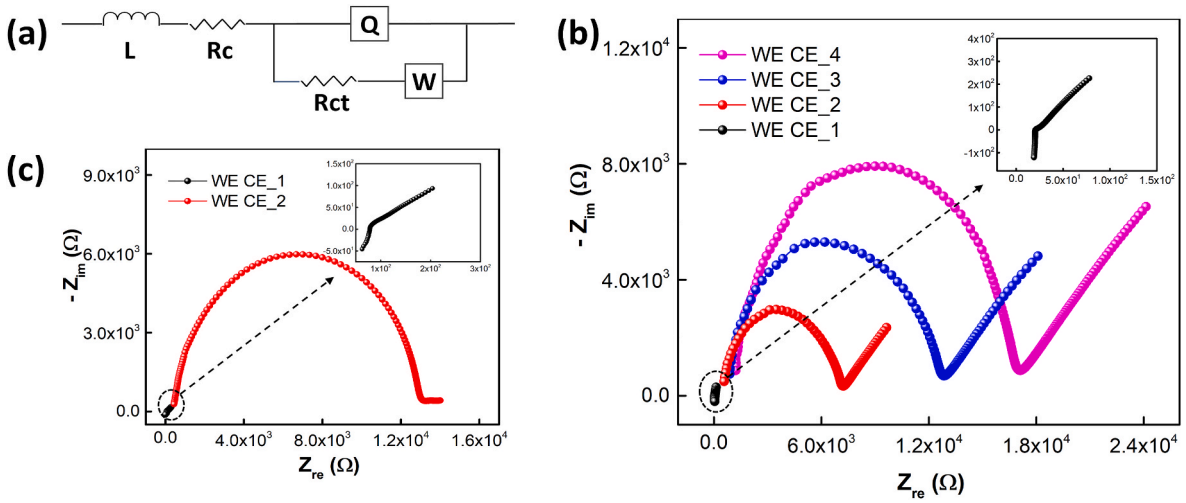

Fig. 5. (a) Equivalent circuit diagram. (b) Nyquist plots of NP-μFEC obtained at different CE positions. (c) Nyquist plots of P-μFEC obtained at different CE positions. The solution is $[Fe(CN)_6]^{3-/4-}$ (0.01 M) in KCl (1 M).

diffusion rate [3,46]. R_{ct} and *W* are modeled parallel to *Q* as co-occurring phenomena [3,45,46]. The equivalent circuit is fitted using the ZSimpWin software (Fig. S5).

During EIS measurements, the CE is moved from CE_1 to CE_4. The corresponding EIS spectra (Nyquist curve) are shown in Fig. 5(b). Significant differences in the impedance spectra are observed during the stepwise movement of the CE. When the CE is located at CE_1 (d_{cw} = ~10 μm, the height of the microfluidic channel is ~140 μm), the electron transfer process between the electrode and electrolyte solution is instantaneous, the R_{ct} is almost negligible, and thus the electrochemical response is a nearly straight line, as shown in the inset. However, the shift from CE_1 to CE_2, CE_3, and CE_4 significantly increased R_{ct}. Table S3 gives the details of each element in the equivalent circuit.

3.3.2. P-μFEC EIS

The impedance spectra (Nyquist curve) of the P-μFEC are shown in Fig. 5(c). Based on the established equivalent circuit, we did the circuit analysis for P-μFEC (Fig. S9). The circuit element's simulated results are summarized in Table S5. Significant differences in the impedance spectra are observed when CE is moved from CE_2 to CE_1. For CE at CE_1, R_{ct} becomes negligible, and thus the impedance response is a nearly straight line, as shown in the inset. This dramatic decrease of R_{ct} makes the electron transfer between the CE and WE more "smooth."

3.4. DPV characterization

DPV is often used for electroanalysis, typically in aqueous solutions, as it is usually an order of magnitude more sensitive than the CV mode [47]. Hence, DPV is used to determine the detection limit (***DL***) of $[Fe(CN)_6]^{3-/4-}$ (a proof-of-concept analyte) to compare the performance of P-μFEC and NP-μFEC as an analytical tool.

3.4.1. NP-μFEC DPV

Fig. 6 compares the differential pulse voltammograms of $[Fe(CN)_6]^{3-/4-}$ obtained at varying electrode configurations. Fig. 6(a) shows a typical voltammogram of the $[Fe(CN)_6]^{3-/4-}$ couple appears at a peak potential (E_{peak}) of *ca.* −15 mV with a full width at half maximum (FWHM) of ~100 mV at WE/CE_1/RE_1. NP-μFEC's ***DL*** is studied for WE/CE_1/RE_1. Unless otherwise indicated, the concentrations referred to here imply the concentrations of $[Fe(CN)_6]^{3-/4-}$ probe. Fig. 6(b) shows an increase in DPV reduction peak currents with the rise of the concentration (Table S7). The calibration curve's linear portion falls from 1 × 10^{-4} to 1 × 10^{-6} M with a high coefficient of determination (R^2) equal to 0.9995, as shown in Fig. 6(c). Therefore, a preliminary value of the ***DL*** can be calculated based on the IUPAC recommended formula (Equation (2)) [48].

$$\boldsymbol{DL} = \frac{K * S_b}{m} \quad (2)$$

Here, *k* is a numerical constant, *m* is the slope of the plot's linear region, and S_b is the standard deviation of the blank or the ordinate intercept standard deviation [49]. According to IUPAC recommendations, a *k* value of 3 corresponds to a 99.87% confidence level [1]. A ***DL*** of ~2.54 × 10^{-6} M is obtained using the above formula for an aqueous $[Fe(CN)_6]^{3-/4-}$ redox couple.

As with the cyclic voltammograms, it is also observed that the variations in the positionings of the RE do not impact the NP-μFEC's DPV response (Fig. 6(d)). For the WE/CE_2/RE_1 configuration, instead of seeing a typical DPV profile, the current (*I*) versus applied voltage (*E*) profile shows a significantly reduced current intensity with a broadened FWHM and a pronounced reduction in the redox features. Similar responses are observed for the configurations WE/CE_3,4/RE_1 (Fig. S15). The DPV results demonstrate that only when the horizontal spacing d_{cw} decreases to ~10 μm (when the CE and WE are interdigitated) that NP-μFEC can give a more pronounced electrochemical response.

3.4.2. P-μFEC DPV

Similarly, the DPV performance of P-μFEC for the aqueous $[Fe(CN)_6]^{3-/4-}$ the probe is studied. Fig. 6(e) shows the DPV results obtained at different CE positions. A well-defined DPV curve shows up only when the CE and WE are interdigitated (CE is fixed at CE_1), with the distance between the adjacent WE and CE fingers being 10 μm. The I_{peak} is observed at E_{peak} = −15 mV with a value of *ca.* −32 μA and an FWHM of ~220 mV. Fig. 6(f) shows a gradual increase in the I_{peak} with the concentration of $[Fe(CN)_6]^{3-/4-}$ couple. The calibration curve's linear portion falls from 1 × 10^{-4} to 1 × 10^{-6} M with an R^2 equal to 0.9998 (Fig. 6(g)). Using Equation (2), we can get a ***DL*** of ~1.8 × 10^{-6} M for aqueous $[Fe(CN)_6]^{3-/4-}$ redox couple. Similarly, as the CE moves to CE_2, the characteristic features of the DPV profile are significantly weakened (Fig. 6(e)).

3.4.3. NP-μFEC vs. P-μFEC

Table S7 summarizes the features of DPV results obtained from the NP-μFEC and P-μFEC. Through careful comparison, two representative differences are outlined here:

(i) **Different FWHM behaviors**: In the NP-μFEC, despite the changes of $[Fe(CN)_6]^{3-/4-}$ concentration in the analyte solution (from 6 × 10^{-4} to 1 × 10^{-5} M), the FWHM of the NP-μFEC remains at a relatively stable value (~100 mV). In contrast, the value of FWHM in P-μFEC experiences a gradual decrease as [Fe

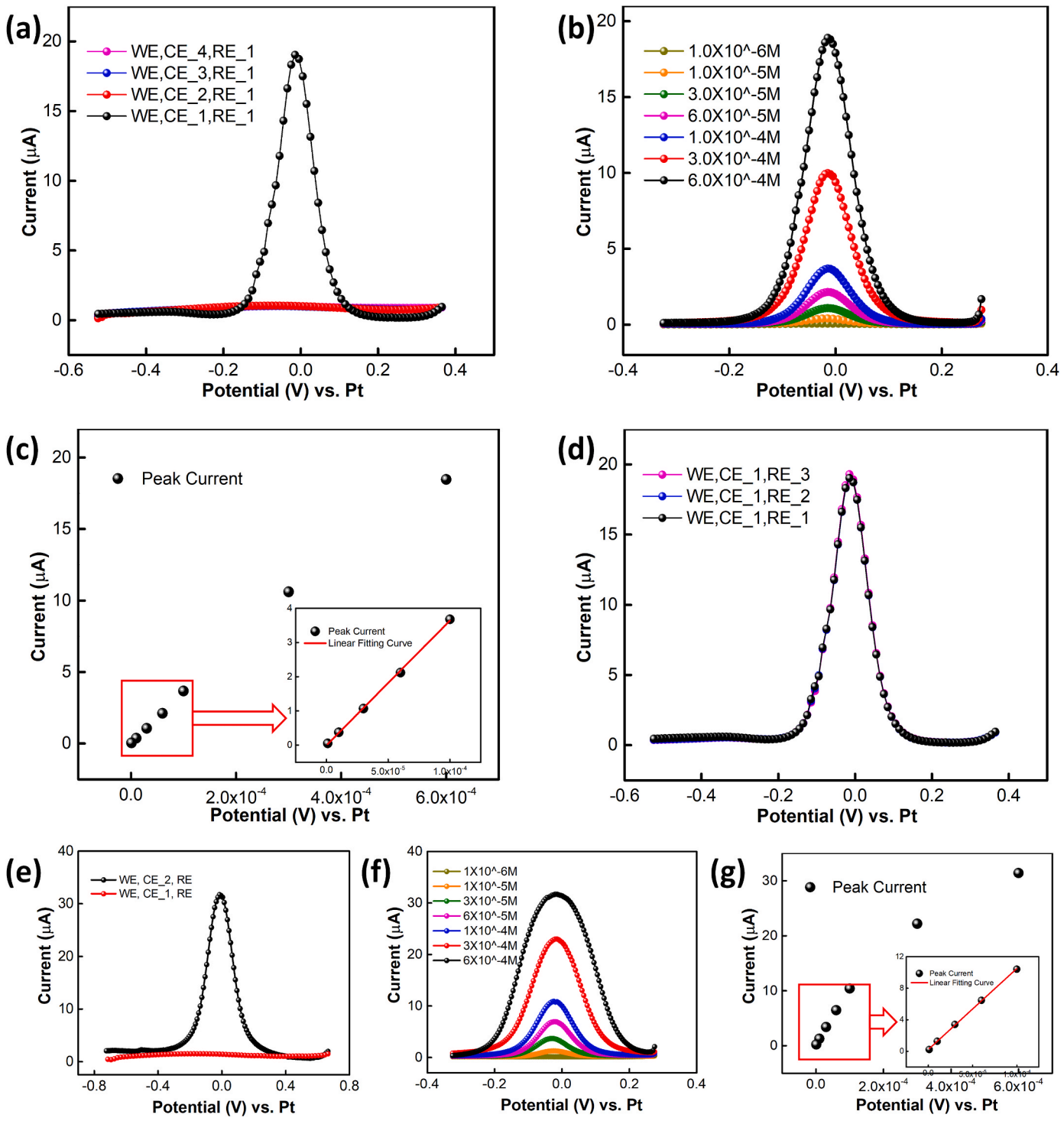

Fig. 6. Results (a)–(d) are the DPV results obtained based on NP-μFEC. (a) DPV results obtained at different CE positions. (b) DPV results obtained using different concentrations of $[Fe(CN)_6]^{3-/4-}$ redox couple. (c) Peak currents for $[Fe(CN)_6]^{3-/4-}$ redox process as a function of increasing $[Fe(CN)_6]^{3-/4-}$ concentration from 1×10^{-4} M to 1×10^{-6} M (linear working range). The equation of the fitting line: Peak current I_{peak} (μA) = −364683.2 × Conc (M) - 0.0068; $R^2 = 0.9995$. (d) DPV results obtained at different RE positions. Results (e)–(g) are the DPV results obtained based on P-μFEC. (e) DPV results obtained at different CE positions. (f) DPV results obtained from different concentrations of the $[Fe(CN)_6]^{3-/4-}$ redox couple. (g) Peak currents for the $[Fe(CN)_6]^{3-/4-}$ redox process with a function of increasing $[Fe(CN)_6]^{3-/4-}$ concentration. From 1×10^{-4} M to 1×10^{-6} M (linear working range) the equation of the fitting line: Peak current I_{peak} (μA) = −103580.64 × Conc (M) + 0.238; $R^2 = 0.9998$. The solution used here for (a), (d), and (e) is $[Fe(CN)_6]^{3-/4-}$ (6×10^{-4} M) in KCl (1 M).

$(CN)_6]^{3-/4-}$ concentration declines. The difference in the FWHM between the NP-μFEC and P-μFEC is probably due to the different dominating electrochemical processes for each (semi-infinite/planar diffusion in NP-μFEC vs. radial diffusion in P-μFEC).

(ii) **Different electric current behavior**: Compared to P-μFEC, a slower decrease in the I_{peak} is observed in NP-μFEC, as illustrated in Fig. S16. P-μFEC has a smaller ***DL*** value. (~1.8×10^{-6} M) than the NP-μFEC device (~2.54×10^{-6} M). Though the transition of μE arrays from coplanar distribution to non-planar distribution

increases ions' diffusion distance, it does not affect the electrochemical performance of NP-μFEC as an electrochemical sensor working in the DC modes.

3.5. NP-μFEC for detection of heavy metal ions in aqueous matrices

NP-μFEC is used to detect heavy metal ions in aqueous solutions. It is expected that with the continual increase in the channel height, the enlarged diffusion distance of ions should deteriorate the NP-μFEC's device performance leading to decreased sensitivity (increased ***DL***). However, the ***DL*** to aqueous $[Fe(CN)_6]^{3-/4-}$ redox probe in NP-μFEC has an anomalous change with the height of the channel, as shown in Fig. 7 (a). NP-μFEC experiences higher sensitivity (lowered ***DL***) until the fluid channel height equals 420 μm. Post 420 μm, the sensitivity decreases (an increase in ***DL***) with an increase in channel height. The ***DL*** is lower at 420 μm from 140 μm by about 46%. We hypothesize that this is due to two possible competing mechanisms. For NP-μFECs, the ratio of the analyte volume in the channel compared to the total electrode surface is approximately the channel height. It has been shown elsewhere that consumption of the analyte by the electrochemical reaction rapidly changes the analyte concentration, affecting the signal magnitude [4, 50]. Hence with the increase in the height of the microfluidic channel, as the amount of analyte in the channel increases, the ***DL*** should decrease. However, the diffusion distance increases with increasing height, which should increase the ***DL*** [51,52]. Hence it can be hypothesized that as the channel height increases from 140 to 420 μm, the ***DL*** decreases due to an increase in the total amount of analyte in the neighborhood, with a corresponding increase in measurement sensitivity. In contrast, beyond 420 μm, the ***DL*** increases again due to the increase in diffusion length. Thus, the lowest ***DL*** is observed at 420 μm for the given electrode and channel geometry. Therefore, the increase in ions overcomes the increased diffusion distance leading to lowered ***DLs*** till the height of the channel reaches 420 μm in NP-μFEC. Beyond this height, the ***DL*** increases as the diffusion distance increases.

Therefore, an NP-μFEC with a height of 420 μm is employed for the rest of the heavy metals' detection work (Fig. 7(b)). Three common heavy metals (Copper (Cu), Iron (Fe), and Mercury (Hg)) and ($[Ru(bpy)_3]^{2+}$) are analyzed. DPV results are demonstrated in Figs. S17 and S18. A detailed, comprehensive study of the reproducibility, sensitivity and selectivity of our NP-μFEC will be done in future work as it is beyond the scope of this paper. Here, the signal-to-noise (SNR) is calculated as the peak current divided by half of the fluctuation in the baseline reading from the pure KCl solution [53]. Using Equation (2), the theoretical DL for Cu^{2+}, Fe^{3+}, Hg^{2+}, and ($[Ru(bpy)_3]^{2+}$) is 30.5± 9.5 μg L^{-1} (SNR ~ 2.1), 181±58.5 μg L^{-1} (SNR ~ 2.0), 12.4± 1.95 μg L^{-1} (SNR ~ 5.0), 83±9 μg L^{-1} (SNR ~ 2.7), respectively, which meets EPA's water contamination level for Cu, Fe (1300 μg L^{-1}, 300 μg L^{-1}, respectively) and is close to the EPA level for Hg (2 μg L^{-1}). Therefore, this demonstrates that the cost-effective, simple fabrication of NP-μFEC can be a new electrochemical analytical tool for other research groups.

4. Conclusions

An assembly of non-planar interdigitated microelectrodes (NP-IDμE) is introduced in this work. The fabrication of NP-IDμE-based microfluidic electrochemical cell (NP-μFEC) and its electrochemical characteristics are studied. The reported NP-μFEC has many advantages over the classical conventional P-μFEC. NP-IDμE, even with non-planar electrode geometry, is easy to assemble with an enhanced three-dimensional (3D) electric field and a relatively high SNR. The convenient fabrication process and the 3D electric field feature NP-μFEC more attractive as an electrochemical tool, whether working in the AC (EIS) or DC (CV and DPV, among others) detection modes.

Electrochemical characterizations (CV, DPV, and EIS) are carried out to illustrate, examine and fundamentally understand the electrochemical behaviors of the NP-μFEC. The effect of the spatial orientation of the μE arrays on the electrochemical behavior is studied in detail. The representative findings are summarized here:

(**i**) From the CV tests, for the NP-μFEC (when the counter electrode (CE) and the working electrode (WE) are interdigitated), the electrochemical process is predominantly controlled by semi-infinite diffusion, which differs from the radial diffusion in the P-μFEC. This enables NP-μFEC to more easily interrogate the valuable information related to redox processes, while P-μFEC is challenging.
(**ii**) The effect of the distance between the electrodes (WE, CE, and reference electrode (RE)) and their positions are carefully studied. CV studies show that the inserted RE position's change does not affect the final electrochemical performance of NP-μFEC. However, the spacing between the CE and WE significantly affects the electrochemical performance.
(**iii**) Finite element analysis (FEA) simulation results demonstrate that for the NP-μFEC, most of the cross-section area of the microchannel layer (~66.00%) falls in a relatively strong electric field intensity (I_{EF}) range (from 9×10^3 to 6×10^3 V m^{-1}). However, for the P-μFEC, most of its channel (~75.77%) falls in a relatively weak I_{EF} interval (<3×10^3 V m^{-1}).
(**iv**) NP-μFEC shows excellent performance to aqueous $[Fe(CN)_6]^{3-/4-}$ redox couple. Furthermore, DPV tests show that the NP-μFEC has a similar detection limit (***DL***) (~2.54×10^{-6} M) to that (~1.8×10^{-6} M) in the P-μFEC.
(**v**) Interestingly, an anomalous lowering of the ***DL*** is observed in NP-μFEC with an increase in channel height to a critical height of 420 μm. An NP-μFEC with a channel height of 420 μm is employed for heavy metal detection. ***DL*** for Cu^{2+} (30.5 ±9.5 μg L^{-1}) and Fe^{3+} (181±58.5 μg L^{-1}) that meet the EPA recommended limits

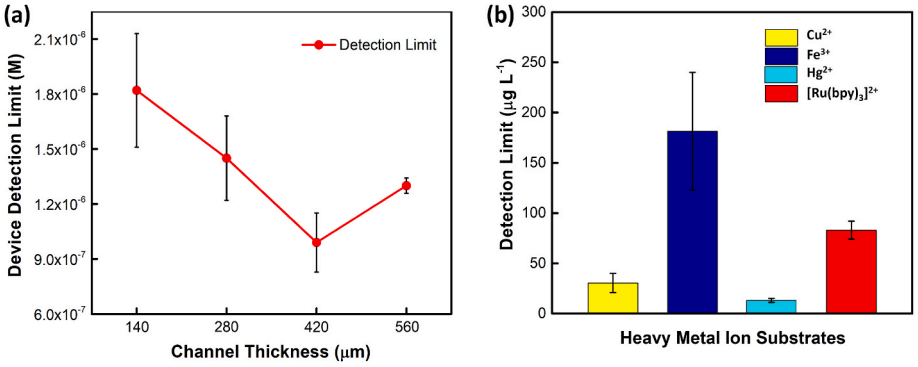

Fig. 7. (a) ***DL*** to aqueous $[Fe(CN)_6]^{3-/4-}$ redox probe based on NP-μFEC using different channel thickness. ***DL*** equals 1.82×10^{-6} (M), 1.45×10^{-6} (M), 9.9×10^{-7} (M), 1.3×10^{-6} (M) when the channel thickness is 140 μm, 280 μm, 420 μm, 560 μm, respectively. (b) Theoretical ***DL*** results for different metals (Cu, Fe, Hg) or metal compound ($[Ru(bpy)_3]^{2+}$) based on NP-μFEC (thickness = 420 μm).

demonstrate that cost-effective, simple fabrication of NP-μFEC can be a new analytical tool for other research groups.

The cumulative results demonstrate the NP-μFEC's general effectiveness for efficient probing electrochemical properties of electroactive analytes. This provides the promise of NP-μFEC as a lab-on-a-chip microfluidic platform for sensitive electrochemical analysis and detection of analytes' where samples are limited in volume.

CRediT authorship contribution statement

Zhenglong Li: performed Experiments, Writing – original draft, Conceptualization. **Yu-Hsuan Cheng:** performed Writing and Editing. **Charmi Chande:** performed Writing and Editing. **Sayandev Chatterjee:** performed Writing and Editing. **Sagnik Basuray:** performed, Writing – review & editing, Conceptualization.

Declaration of competing interest

The authors declare that they have no known competing financial interests or personal relationships that could have appeared to influence the work reported in this paper.

Data availability

Data will be made available on request.

Acknowledgments

This manuscript is supported by Sagnik Basuray's NSF grant # 1751759, Career: "ASSURED" electrochemical platform for multiplexed detection of Cancer Biomarker Panel using Shear Enhanced Nanoporous Capacitive Electrodes and a New Jersey Health Foundation Grant, # PC 54–20, "ESSENCE - A Selective and Sensitive Electrochemical POC Platform for Liquid Biopsy" and an ESTCP grant, #ER21-5101, "Field-Scale Demonstration of a Novel Real-Time Sensor for PFAS." In addition, the authors acknowledge the valuable input from Dr. Radha Kishan Motkuri.

Appendix A. Supplementary data

Supplementary data to this article can be found online at https://doi.org/10.1016/j.aca.2022.340488.

References

[1] S. Chatterjee, M.S. Fujimoto, Y.H. Cheng, R. Kargupta, J.A. Soltis, R.K. Motkuri, S. Basuray, Improving the sensitivity of electrochemical sensors through a complementary luminescent mode: a new spectroelectrochemical approach, Sensor. Actuator. B Chem. 284 (2019) 663–674.

[2] J.S. Daniels, N. Pourmand, Label-free impedance biosensors: opportunities and challenges, Electroanalysis, Int. J. Devoted Fund. Practical Aspects Electroanalysis, 19 (2007) 1239–1257.

[3] Z. Li, Y.-H. Cheng, L. Feng, J. Neil, R.M.P. Antonio, M. Rahman, J. Yang, S. Azizighannad, S. Mitra, S. Basuray, Communication—electrochemical impedance signature of a non-planar, interdigitated, flow-through, porous, carbon-based microelectrode, J. Electrochem. Soc. 166 (2019) B1669–B1672.

[4] J. Min, A.J. Baeumner, Characterization and optimization of interdigitated ultramicroelectrode arrays as electrochemical biosensor transducers, Electroanalysis: Int. J. Devoted Fund. Practical Aspects Electroanalysis, 16 (2004) 724–729.

[5] M.B. Rooney, D.C. Coomber, A.M. Bond, Achievement of near-reversible behavior for the [Fe (CN) 6] 3-/4-redox couple using cyclic voltammetry at glassy carbon, gold, and platinum macrodisk electrodes in the absence of added supporting electrolyte, Anal. Chem. 72 (2000) 3486–3491.

[6] C. Lee, F.C. Anson, Inhibition of the electroreduction of Fe (CN) 3-6 at microelectrodes in the absence of supporting electrolyte. Mediation of the inhibited reduction by methyl viologen, J. Electroanal. Chem. Interfacial Electrochem. 323 (1992) 381–389.

[7] M. Ciszkowska, Z. Stojek, Voltammetry in solutions of low ionic strength. Electrochemical and analytical aspects, J. Electroanal. Chem. 466 (1999) 129–143.

[8] M. Nishizawa, I. Uchida, Microelectrode-based characterization systems for advanced materials in battery and sensor applications, Electrochim. Acta 44 (1999) 3629–3637.

[9] J. Kawiak, P.J. Kulesza, Z. Galus, A search for conditions permitting model behavior of the Fe (CN) 3−/4− 6 system, J. Electroanal. Chem. Interfacial Electrochem. 226 (1987) 305–314.

[10] A. Bratov, N. Abramova, J. Ramón-Azcón, A. Merlos, F. Sánchez-Baeza, M.-P. Marco, C. Domínguez, Characterisation of the interdigitated electrode array with tantalum silicide electrodes separated by insulating barriers, Electrochem. Commun. 10 (2008) 1621–1624.

[11] P. Van Gerwen, W. Laureyn, W. Laureys, G. Huyberechts, M.O. De Beeck, K. Baert, J. Suls, W. Sansen, P. Jacobs, L. Hermans, Nanoscaled interdigitated electrode arrays for biochemical sensors, Sensor. Actuator. B Chem. 49 (1998) 73–80.

[12] S.R.A. Ruth, V.R. Feig, M.-g. Kim, Y. Khan, J.K. Phong, Z. Bao, Flexible Fringe Effect Capacitive Sensors with Simultaneous High−Performance Contact and Non−Contact Sensing Capabilities, Small Structures, 2020, 2000079.

[13] Y.-H. Cheng, P.A.R. Moura, L. Zhenglong, L. Feng, S. Arokiam, J. Yang, M. Hariharan, S. Basuray, Effect of electrode configuration on the sensitivity of nucleic acid detection in a non-planar, flow-through, porous interdigitated electrode, Biomicrofluidics 13 (2019), 064118.

[14] Y.-H. Cheng, R. Kargupta, D. Ghoshal, Z. Li, C. Chande, L. Feng, S. Chatterjee, N. Koratkar, R.K. Motkuri, S. Basuray, ESSENCE–A rapid, shear-enhanced, flow-through, capacitive electrochemical platform for rapid detection of biomolecules, Biosens. Bioelectron. 182 (2021), 113163.

[15] H. Sugime, T. Ushiyama, K. Nishimura, Y. Ohno, S. Noda, An interdigitated electrode with dense carbon nanotube forests on conductive supports for electrochemical biosensors, Analyst 143 (2018) 3635–3642.

[16] A. Abellán-Llobregat, L. Vidal, R. Rodríguez-Amaro, Á. Berenguer-Murcia, A. Canals, E. Morallon, Au-IDA microelectrodes modified with Au-doped graphene oxide for the simultaneous determination of uric acid and ascorbic acid in urine samples, Electrochim. Acta 227 (2017) 275–284.

[17] A. Bratov, J. Ramón-Azcón, N. Abramova, A. Merlos, J. Adrian, F. Sánchez-Baeza, M.-P. Marco, C. Domínguez, Three-dimensional interdigitated electrode array as a transducer for label-free biosensors, Biosens. Bioelectron. 24 (2008) 729–735.

[18] E.W. Young, D.J. Beebe, Fundamentals of microfluidic cell culture in controlled microenvironments, Chem. Soc. Rev. 39 (2010) 1036–1048.

[19] D. Daniel, I.G. Gutz, Microfluidic cells with interdigitated array gold electrodes: fabrication and electrochemical characterization, Talanta 68 (2005) 429–436.

[20] Y.H. Cheng, D. Barpaga, J.A. Soltis, V. Shutthanandan, R. Kargupta, K.S. Han, B. P. McGrail, R.K. Motkuri, S. Basuray, S. Chatterjee, Metal-organic framework-based microfluidic impedance sensor platform for ultrasensitive detection of perfluorooctanesulfonate, ACS Appl. Mater. Interfaces 12 (2020) 10503–10514.

[21] S. Basuray, S. Senapati, A. Aijian, A.R. Mahon, H.C. Chang, Shear and AC field enhanced carbon nanotube impedance assay for rapid, sensitive, and mismatch-discriminating DNA hybridization, ACS Nano 3 (2009) 1823–1830.

[22] A. Saha, S. Mitra, Microfluidics and Nanofluidics Handbook: Chemistry, Physics, and Life Science Principles, Taylor & Francis Group, 2012.

[23] F. Zhang, J. Liu, I. Ivanov, M.C. Hatzell, W. Yang, Y. Ahn, B.E. Logan, Reference and counter electrode positions affect electrochemical characterization of bioanodes in different bioelectrochemical systems, Biotechnol. Bioeng. 111 (2014) 1931–1939.

[24] Z. Li, J. Ni, S. Zhang, C. Li, Y. Du, Y. Zhang, H. Cai, J. Li, J. Zhang, Effect of incorporation of highly-ordered a-Ge: H nanoparticles on the performance of perovskite solar cells, Micro & Nano Lett. 13 (2018) 1111–1116.

[25] S. Cheng, H. Liu, B.E. Logan, Increased performance of single-chamber microbial fuel cells using an improved cathode structure, Electrochem. Commun. 8 (2006) 489–494.

[26] G. Hsieh, T.O. Mason, E. Garboczi, L. Pederson, Experimental limitations in impedance spectroscopy: Part III. Effect of reference electrode geometry/position, Solid State Ionics 96 (1997) 153–172.

[27] R.A. da Silva, E.G. de Almeida, A.C. Rabelo, A.T. da Silva, L.F. Ferreira, E. M. Richter, Three electrode electrochemical microfluidic cell: construction and characterization, J. Braz. Chem. Soc. 20 (2009) 1235–1241.

[28] Y. Li, W. Van Roy, L. Lagae, P.M. Vereecken, Effects of counter electrode induced redox cycling on Fe (III) reduction within microfluidic electrochemical cells, J. Electrochem. Soc. 161 (2014) E128.

[29] H. Tantang, J. Xiao, J. Wei, M.B.E. Chan-Park, L.J. Li, Q. Zhang, Low–cost and ultra–strong p–type doping of carbon nanotube films by a piranha mixture, Eur. J. Inorg. Chem. (2011) 4182–4186, 2011.

[30] C. Amatore, N. Da Mota, C. Sella, L. Thouin, Theory and experiments of transport at channel microband electrodes under laminar flows. 1. Steady-state regimes at a single electrode, Anal. Chem. 79 (2007) 8502–8510.

[31] S. Konopka, B. McDuffie, Diffusion coefficients of ferri-and ferrocyanide ions in aqueous media, using twin-electrode thin-layer electrochemistry, Anal. Chem. 42 (1970) 1741–1746.

[32] H.-C. Chang, C.-C. Wu, S.-J. Ding, I.-S. Lin, I.-W. Sun, Measurement of diffusion and partition coefficients of ferrocyanide in protein-immobilized membranes, Anal. Chim. Acta 532 (2005) 209–214.

[33] K.B. Oldham, N.P. Stevens, Uncompensated resistance. 2. The effect of reference electrode nonideality, Anal. Chem. 72 (2000) 3981–3988.

[34] J.-M. Savéant, Elements of Molecular and Biomolecular Electrochemistry, Willey-VCH, New Jersey, 2006.

[35] J.C. Myland, K.B. Oldham, Uncompensated resistance. 1. The effect of cell geometry, Anal. Chem. 72 (2000) 3972–3980.

[36] N. Elgrishi, K.J. Rountree, B.D. McCarthy, E.S. Rountree, T.T. Eisenhart, J. L. Dempsey, A practical beginner's guide to cyclic voltammetry, J. Chem. Educ. 95 (2018) 197–206.
[37] S. Hwang, C.N. LaFratta, V. Agarwal, X. Yu, D.R. Walt, S. Sonkusale, CMOS microelectrode array for electrochemical lab-on-a-chip applications, IEEE Sensor. J. 9 (2009) 609–615.
[38] R.O. Kadara, N. Jenkinson, C.E. Banks, Characterization and fabrication of disposable screen printed microelectrodes, Electrochem. Commun. 11 (2009) 1377–1380.
[39] C.A. Schroll, S. Chatterjee, W.R. Heineman, S.A. Bryan, Semi-infinite linear diffusion spectroelectrochemistry on an aqueous micro-drop, Anal. Chem. 83 (2011) 4214–4219.
[40] Y. Yang, C. Li, L. Yin, M. Liu, Z. Wang, Y. Shu, G. Li, Enhanced charge transfer by gold nanoparticle at DNA modified electrode and its application to label-free DNA detection, ACS Appl. Mater. Interfaces 6 (2014) 7579–7584.
[41] E. Kostal, S. Kasemann, C. Dincer, S. Partel, Impedimetric Characterization of Interdigitated Electrode Arrays for Biosensor Applications, Multidisciplinary Digital Publishing Institute Proceedings, 2018, p. 899.
[42] S. Ismail, N. Mahmood, M.A. Razak, Optimization of interdigitated electrodes in electric field distribution and thermal effect, J. Telecommun. Electron. Comput. Eng. 9 (2017) 85–89.
[43] K.V. Singh, A.M. Whited, Y. Ragineni, T.W. Barrett, J. King, R. Solanki, 3D nanogap interdigitated electrode array biosensors, Anal. Bioanal. Chem. 397 (2010) 1493–1502.
[44] A. Bratov, S. Brosel-Oliu, N. Abramova, Label-Free Impedimetric Biosensing Using 3D Interdigitated Electrodes, Label-Free Biosensing, Springer2017, pp. 179-198.
[45] S. Ding, C. Mosher, X.Y. Lee, S.R. Das, A.A. Cargill, X. Tang, B. Chen, E. S. McLamore, C. Gomes, J.M. Hostetter, Rapid and label-free detection of interferon gamma via an electrochemical aptasensor comprising a ternary surface monolayer on a gold interdigitated electrode array, ACS Sens. 2 (2017) 210–217.
[46] M.S. Abouzari, F. Berkemeier, G. Schmitz, D. Wilmer, On the physical interpretation of constant phase elements, Solid State Ionics 180 (2009) 922–927.
[47] G. Hussain, D.S. Silvester, Comparison of voltammetric techniques for ammonia sensing in ionic liquids, Electroanalysis 30 (2018) 75–83.
[48] G.L. Long, J.D. Winefordner, Limit of detection. A closer look at the IUPAC definition, Anal. Chem. 55 (1983) 712A–724A.
[49] A. Shrivastava, V.B. Gupta, Methods for the determination of limit of detection and limit of quantitation of the analytical methods, Chronicles Young Sci. 2 (2011) 21.
[50] O. Niwa, Y. Xu, H.B. Halsall, W.R. Heineman, Small-volume voltammetric detection of 4-aminophenol with interdigitated array electrodes and its application to electrochemical enzyme immunoassay, Anal. Chem. 65 (1993) 1559–1563.
[51] J. Zhao, Y.Z. Zhang, F. Zhang, H. Liang, F. Ming, H.N. Alshareef, Z. Gao, Partially reduced holey graphene oxide as high performance anode for sodium–ion batteries, Adv. Energy Mater. 9 (2019), 1803215.
[52] C.R. McNeill, S. Westenhoff, C. Groves, R.H. Friend, N.C. Greenham, Influence of nanoscale phase separation on the charge generation dynamics and photovoltaic performance of conjugated polymer blends: balancing charge generation and separation, J. Phys. Chem. C 111 (2007) 19153–19160.
[53] M.P. Klein, G.W. Barton Jr., Enhancement of signal–to–noise ratio by continuous averaging: application to magnetic resonance, Rev. Sci. Instrum. 34 (1963) 754–759.